Received: 25 February 2022 | Revised: 29 April 2022 | Accepted: 1 May 2022 | Published on: 24 May 2022

DOI: 10.1002/gamm.202200012

ORIGINAL PAPER

High-order modeling of interface interactions using level sets

Nico Fleischmann[1] | **Josef M. Winter**[1] | **Stefan Adami**[2] | **Nikolaus A. Adams**[1,2]

[1]Technical University of Munich, School of Engineering & Design, Department Engineering Physics and Computation, Chair of Aerodynamics and Fluid Mechanics, Garching, Germany

[2]Technical University of Munich, Munich Institute of Integrated Materials, Energy and Process Engineering (MEP), Garching, Germany

Correspondence
Stefan Adami, Technical University of Munich, Munich Institute of Integrated Materials, Energy and Process Engineering (MEP), Lichtenbergstr. 4a, 85748 Garching, Germany.
Email: stefan.adami@tum.de

Funding information
European Research Council, Grant/Award Number: 667483

Abstract

Most technological advancements in medicine, process and energy engineering, life and food science, mobility and environmental engineering involve mastering fluid mechanical effects. In particular, compressible flow physics including shockwaves and phase-interface interactions exhibit multi-scale phenomena spanning several orders of magnitude upwards from nanometer and nanosecond time scales. Clearly, detailed analysis of such effects is impossible by means of experimental techniques. On the contrary, numerical modeling and simulations allow to capture the aforementioned mechanisms and provide non-invasive access to *any* quantity of interest. Yet, the complex fluid physics require powerful computational methods utilizing recent advancements for high-order schemes. In this work, we provide an overview on latest high-order low-dissipation schemes using level sets to model discontinuous phase-interface interactions.

KEYWORDS

compressible flows, high-order schemes, level set, multi-resolution

1 | INTRODUCTION

The dynamics of fluids can be considered as one of the most complex physical problems to solve. Although the Navier–Stokes equations as fundamental governing equations were formulated in the early 1800's, the existence and uniqueness of its solution is yet to be proven and defines one of the so-called Millennium problems[1] of the Clay Mathematics Institute in Cambridge (Massachusetts). Except for very limited cases, experiments and numerical simulations offer the only possibility to find valid solutions for complex fluid mechanical problems. In comparison with experiments, computational fluid mechanics are appealing due to the modeling capabilities and access to quantitative simulation data. Different to reality, virtual experiments in the form of numerical simulations allow to study isolated physical phenomena or visualize and monitor quantities of interest at arbitrary locations. Non-invasive measurement is one of the key advantages in numerical simulations. Unfortunately, the formulation of a generalized numerical model for the Navier–Stokes equations is not appropriate, as different physical phenomena require fundamentally different solution techniques. As very general survey, flow solver can be classified as *incompressible* or *compressible*, with further differentiation in *single-phase* and *multi-phase* flows. Compressible multi-phase flows can be considered as most complex within these categories when it comes to numerical modeling. Physically, multi-phase flows are governed by additional effects such as surface tension and can require different constitutive laws for individual phases. Compressible effects imply generation and advection of shockwaves as quasi-discontinuities from a discretization point-of-view. Also, effects like the

[1]http://www.claymath.org/millennium-problems

The copyright line for this article was changed on 23 September 2022 after original online publication.

baroclinic vorticity generation introduce complex flow structures when pressure waves interact with density gradients. Last but not least, numerical methods tend to oscillatory or unstable results for flow field variations differing in orders of magnitude like in density for water-air systems.

In this overview, we present some of our major advancements for high-order schemes to model interface-interaction driven compressible multi-phase flows. The available methods for may be roughly grouped by approaches that strictly enforce the immiscibility condition (sharp-interface methods), and approaches that allow the interface to be smeared out over few computational cells (diffuse-interface methods). While sharp-interface methods are considered to be highly accurate, these methods often reveal a significant algorithmic complexity and computational overhead. Certainly, diffuse interface methods show an attractive computational performance and are often simple to implement. However, the latter may suffer from the diffuse interface representation by violating the immiscibility assumption. As a consequence, the modeling of surface tension forces poses additional difficulties. In this work, we strictly rely on the sharp-interface description and present latest results for advanced level-set methods in combination with low-dissipation schemes.

We have developed the advanced simulation framework *ALPACA* [17,19] to simulate accurately multi-physics problems of compressible fluid dynamics giving access to breakthrough innovations and high-impact technologies, ranging from shock-driven nanoparticle reactors to non-invasive shock-mediated low-impact cancer therapies. Based on a level-set multiphase formulation, ALPACA is capable of predicting highly complex interface-interaction mechanisms with discontinuous flow states. Computational efficiency is achieved by a fully MPI-parallelized multi-resolution compression methodology.

In the following, we provide an overview on essential modeling aspects and present some illustrative demonstration examples for the capabilities of ALPACA. For more details, we refer to the relevant original publications in the respective sections.

2 | NUMERICAL MODEL

2.1 | Governing equations

The governing equations including viscous and capillary forces read in vector notation

$$\frac{\partial \mathbf{U}}{\partial t} + \nabla^T \cdot \mathbf{F} + \nabla^T \cdot \mathbf{F}_v + \nabla^T \cdot \mathbf{F}_q = \mathbf{X} \tag{1}$$

with

$$\mathbf{U} = \begin{pmatrix} \rho \\ \rho\mathbf{u} \\ E \end{pmatrix}, \quad \mathbf{F} = \begin{pmatrix} \mathbf{u}\rho \\ \rho\mathbf{u} \otimes \mathbf{u} + p\mathbf{I} \\ \mathbf{u}(E+p) \end{pmatrix}, \quad \mathbf{F}_v = \begin{pmatrix} 0 \\ \mathbf{T} \\ \mathbf{T} \cdot \mathbf{u} \end{pmatrix}, \quad \text{and} \quad \mathbf{F}_q = \begin{pmatrix} 0 \\ 0 \\ \mathbf{q} \end{pmatrix},$$

denoting the vector of conservative states, the convective flux vector, the viscous flux vector, and the heat flux vector, respectively. Here, ρ denotes the density, t the time, $\mathbf{u}$ the velocity vector, p the pressure, $\mathbf{I}$ the identity matrix, $\mathbf{T}$ the Cauchy stress tensor, and E the total energy $E = \rho e + \frac{1}{2}\rho\mathbf{u} \cdot \mathbf{u}$, composed of the internal energy (ρe) and the kinetic energy ($1/2\rho\mathbf{u} \cdot \mathbf{u}$). Heat fluxes are considered by $\mathbf{q} = -\kappa\nabla T$, with the thermal conductivity κ and temperature T. The vector $\mathbf{X}$ denotes exchange terms between two phases including capillary, viscous effects, and thermal conduction. The system of equations is closed by the stiffened-gas equation-of-state (EOS) $p = (\gamma - 1)\rho e - \gamma p_\infty$, where the ratio of specific heats γ and the background pressure p_∞ are empirically determined parameters. The stiffened-gas EOS has been widely used in simulations with multiple immiscible compressible fluids. We use this EOS for both fluids air and water.

2.2 | Finite-volume method

The levelset approach allows for an independent treatment of each fluid phase. The time evolution of the vector of cell-averaged conservative states $\bar{\mathbf{U}}$ is then evaluated for each phase separately using the classical finite volume approach

$$\frac{d}{dt}\bar{\mathbf{U}}_i = \frac{1}{\Delta x}\left(\mathbf{F}_{i-\frac{1}{2},j,k} - \mathbf{F}_{i+\frac{1}{2},j,k} + \mathbf{G}_{i,j-\frac{1}{2},k} - \mathbf{G}_{i,j+\frac{1}{2},k} + \mathbf{H}_{i,j,k-\frac{1}{2}} - \mathbf{H}_{i,j,k+\frac{1}{2}}\right), \tag{2}$$

where $\Delta x (= \Delta y = \Delta z)$ is the cell size of a uniform Cartesian grid, and **F**, **G**. **H** approximate the cell-face fluxes in x-, y-, and z-direction, respectively. Cells that include more than one phase require an additional levelset treatment as described in detail by Hoppe et al. [19]. A short overview of the levelset procedures is also provided in Section 2.7.

We follow the Godunov's approach [13] and determine the convective face fluxes of Equation (2) via the solution of Riemann problems at the volume-volume interface of neighboring cells. Different classical flux formulations are available in our framework, such as the Roe Riemann solver [33], different types of HLL-type Riemann solver [9,16,39], but also classical Lax–Friedrichs formulations. Further details of improved Riemann solver solvers developed along with this numerical framework are described in Section 2.5. We apply different high-order reconstruction schemes [11,35] to recover minutest details of the investigated flow configurations. The reconstructions are performed in characteristic space to avoid spurious oscillations near discontinuities.

2.3 | Multiresolution compression

The introduction of variable resolution in space in numerical simulations strongly improves the prediction capabilities. Although physically relevant, interfacial structures often do not cover geometrically major parts of the simulation domain. Therefore it is favorable to use highest available grid resolutions only partially in the domain. Here, we employ wavelet-based multiresolution compression (MR) based on the original work of Harten [15]. In comparison to the truncation-error based adaptive mesh refinement (AMR) schemes, MR can achieve larger compression with better error control [4]. We developed an efficient block-based refinement algorithm, that allows for utilizing single instruction multiple data (SIMD) parallelization [18]. Note, we allow arbitrary multi-level jumps in resolution from one block to another. Our tailored MR interacts with the level-set advection by enforcing the highest grid-refinement level in the vicinity of moving fronts. For more details on MR and its implementation in ALPACA, we refer to [19,23].

2.4 | Treatment of floating-point induced disturbances

Modern low-dissipation schemes suffer from floating-point induced disturbances that are no longer sufficiently suppressed by the inherent numerical dissipation of the underlying scheme [5,6,8,31,42]. The effect of symmetry breaking was first connected to floating point round-off errors by Remacle et al. [31], and first systematically controlled by Fleischmann et al. [8]. Alternatively, Dong et al. [5,6] proposed to modify the smoothness indicators of WENO-type schemes to reduce adverse floating-point effects, whereas Wang et al. [42] applied a symmetrization procedure with an active averaging of state values in symmetrically placed cells.

The underlying problem can be traced back to round-of errors in floating-point summations of three or more terms. Multiple procedures in the numerical algorithm include such summations, for example, when the characteristic decomposition is applied for high-order state reconstructions using

$$\mathbf{W} = \mathbf{L} \cdot \mathbf{U} = \mathbf{L}_1 \rho + \mathbf{L}_2 \rho u + \mathbf{L}_3 \rho v + \mathbf{L}_4 \rho w + \mathbf{L}_5 E \tag{3}$$

with $\mathbf{L} = (\mathbf{L}_1, \mathbf{L}_2, \mathbf{L}_3, \mathbf{L}_4, \mathbf{L}_5)$ being the left eigenvector matrix. Indeed, the order of terms then affects the result of this summation within the range of machine precision. Figure 1 shows how the state values in symmetrically placed cells A and B can diverge as a result of this summation, even though the original values were perfectly symmetric. Afterwards, inverse cascade effects may eventually augment differences and lead to large-scale effects, such as symmetry breaking.

Within our flow solver, we apply the generalized procedure of Fleischmann et al. [8] to avoid artificially introduced symmetry breaking. Floating-point induced errors are improved and directional dependencies are diminished via the so-called consistency-ensuring summation procedure

$$S_{consistent} = \frac{1}{2} \left(\max(s_1, s_2, s_3) + \min(s_1, s_2, s_3) \right) \tag{4}$$

with

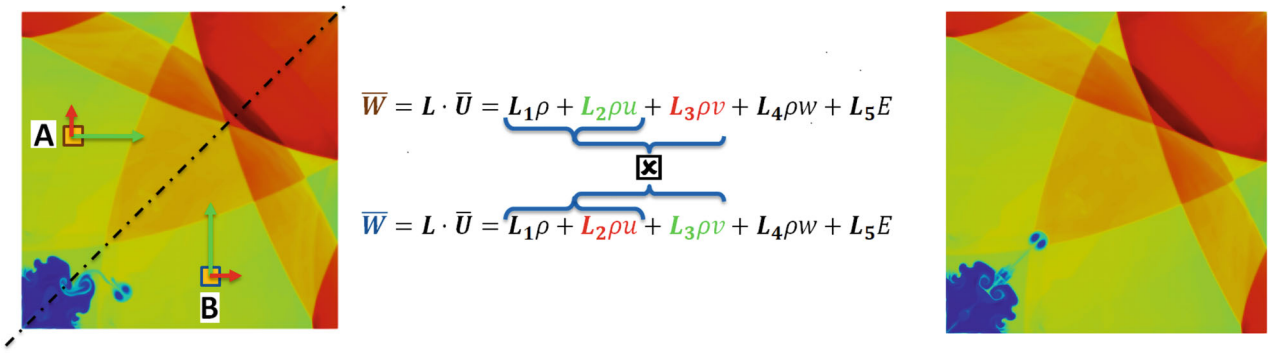

FIGURE 1 Illustration of the asymmetric floating-point evaluation of Equation (3) for two symmetrically placed cells leading to symmetry breaking (left). Directionally consistent summations retain inherent symmetries (right). Reprinted with permissions from the publisher.

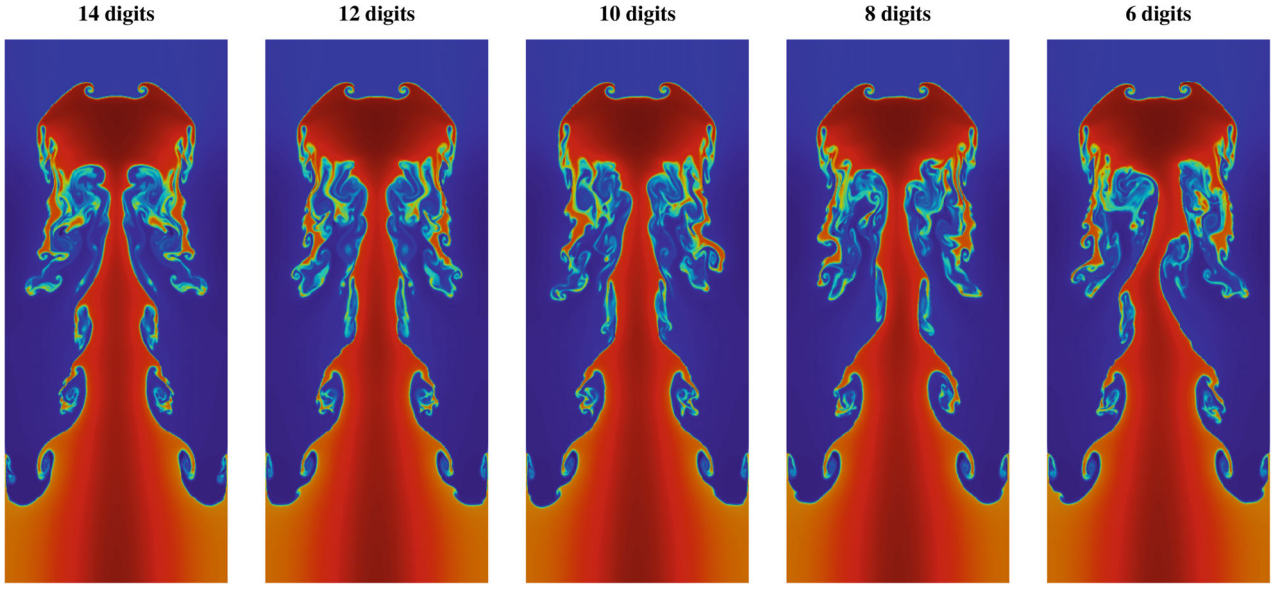

FIGURE 2 Symmetry breaking due to limited representation of π to the given number of digits for a Rayleigh–Taylor instability. Reprinted with permissions from the publisher.

$$\begin{aligned} s_1 &= (a+b)+c, \\ s_2 &= (c+a)+b, \\ s_3 &= (b+c)+a, \end{aligned} \tag{5}$$

where $S_{consistent}$ gives the directionally consistent sum of s_1, s_2, and s_3.

It is important to notice, that even though all procedures within the numerical framework apply consistent floating-point procedures, symmetry breaking can be nevertheless triggered by non-symmetric initial conditions. Figure 2 shows the evolution of Rayleigh–Taylor instabilities with an increasing level of disturbances triggered by insufficient precision of π within the initial pressure. This effect often leads to symmetry breaking in complex multi-component simulations due to the fact that a precise symmetric initialization of the levelset function often is not given.

2.5 | Shock-stable flux functions

Several representatives of widespread low-dissipation Riemann solver types show severe shortcomings when high speed flows are simulated. In cases, where the local Mach number reaches values between 2 and 3 or above, severe disturbances may occur near propagating shock waves. These disturbances considerably limit an accurate prediction of hypersonic

flows. This adverse effect of low-dissipation schemes was first described several decades ago [27,30], and it has been intensively studied since then. An detailed overview of the topic is provided by Rodionov [32].

Most of the available treatments of grid-aligned shock instabilities add a significant amount of numerical dissipation around the shock location to stabilize the shock front. Alternatively, Fleischmann et al. [9,10] proposed simple modifications to the Roe and HLLC flux formulations that stabilize the calculation without adding any additional dissipation to the applied scheme. To the contrary, the numerical dissipation of the proposed Roe-M and HLLC-LM scheme is further reduced as compared to their parent schemes.

The classical Roe formulation [33] gives the following numerical flux function

$$\mathbf{F}^{Roe}_{i+1/2} = \frac{1}{2}\left(\mathbf{F}_{i+1} + \mathbf{F}_i\right) - \frac{1}{2}\mathbf{R}_{i+1}\left|\mathbf{\Lambda}_{i+1}\right|\mathbf{R}^{-1}_{i+1}\left(\mathbf{U}_{i+1} - \mathbf{U}_i\right), \tag{6}$$

where $\mathbf{R}$ and $\mathbf{R}^{-1}$ are the right and the left eigenvector matrices of the Jacobian $\partial\mathbf{F}/\partial\mathbf{U}$, and $\mathbf{\Lambda}$ is the diagonal matrix formed with the eigenvalues

$$\lambda_1 = \hat{u} - \hat{c}, \qquad \lambda_{2,3,4} = \hat{u}, \qquad \lambda_5 = \hat{u} + \hat{c}. \tag{7}$$

The modified Roe-M flux [10] reduces the acoustic contribution to the inherent dissipation of the scheme systematically for low Mach numbers. This is achieved by the simple decrease of acoustic eigenvalues

$$\lambda^{Roe-M}_{1,5} = \hat{u} \pm \min\left(\phi\left|\hat{u}\right|, \hat{c}\right), \qquad \lambda'_{2,3,4} = \hat{u}. \tag{8}$$

If the robustness of the simulation has to be increased, for example, if positivity is violated, it is beneficial to apply the componentwise local Lax–Friedrichs scheme adding only a minor modification to the eigenvalues

$$\begin{aligned}
\lambda^{cLLF-M}_1 &= \max\left(\left|u_i - c'_i\right|, \left|u_{i+1} - c'_{i+1}\right|\right),\\
\lambda^{cLLF-M}_{2,3,4} &= \max\left(\left|u_i\right|, \left|u_{i+1}\right|\right),\\
\lambda^{cLLF-M}_5 &= \max\left(\left|u_i + c'_i\right|, \left|u_{i+1} + c'_{i+1}\right|\right),
\end{aligned} \tag{9}$$

with

$$c'_{i,i+1} = \min\left(\phi\left|u_{i,i+1}\right|, c_{i,i+1}\right). \tag{10}$$

Figure 3 shows the result of the simulation of a $Ma = 6$ shock wave in air interacting with a helium bubble. Three distinct carbuncles deteriorate the shock front when the classical Roe scheme is applied as shown on the left in Figure 3. Instead, the modified Roe-M scheme is able to predict a stable shock front while retaining all other features of the flow. The application of shock-stable schemes reveal similar beneficial behavior in context of the high-speed odd-even decoupling problem originally described by Quirk [30] and kinked Mach stem problems, for example, in context of double-Mach reflections.

The choice of the HLLC flux [16,39] often seems beneficial for high speed flow configurations when compared to the Roe flux. It usually seems less affected by the carbuncle phenomenon and produces only minor disturbances up to high Mach numbers. However, this is only true for moderate grid resolutions and two-dimensional simulations. In case of highly resolved three-dimensional simulations, the classical HLLC solver is also significantly affected by the grid-aligned shock instability as shown in the left part of Figure 4 [9] for an exemplarily simulation of a shock-driven bubble collapse of air in water.

We apply the centralized HLLC flux formulation [9]

$$\mathbf{F}^{HLLC} = \begin{cases} \mathbf{F}_L & \text{if } S_L \geq 0,\\ \mathbf{F}_R & \text{if } S_R \leq 0,\\ \mathbf{F}_* & \text{else} \end{cases} \tag{11}$$

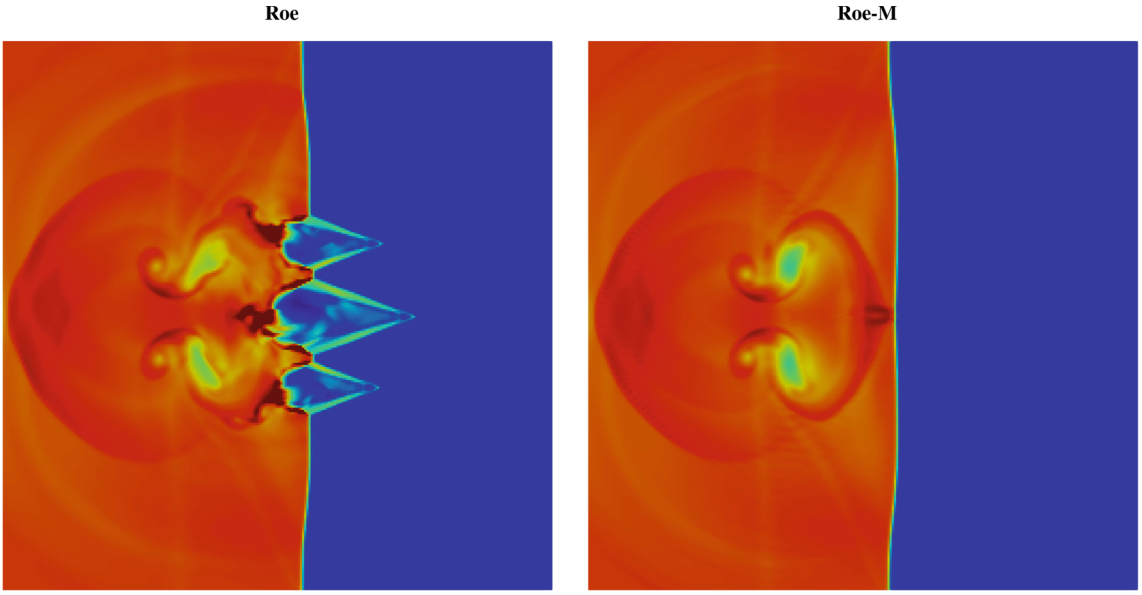

FIGURE 3 Shock interface interaction of a helium bubble in air with (left) and without (right) grid-aligned shock instability

with

$$\mathbf{F}_* = \frac{1}{2}\left(\mathbf{F}_L + \mathbf{F}_R\right) + \frac{1}{2}\left[S_L\left(\mathbf{U}_{*L} - \mathbf{U}_L\right) + |S_*|\left(\mathbf{U}_{*L} - \mathbf{U}_{*R}\right) + S_R\left(\mathbf{U}_{*R} - \mathbf{U}_R\right)\right]. \tag{12}$$

This formulation delivers identical results as the original formulation [39]. However, it allows for a straightforward modification to stabilize grid-aligned shocks also for HLLC-type solvers. The shock-stable HLLC-LM scheme is obtained by the reduction of the acoustic contribution to dissipation using the modified nonlinear signal speed estimates

$$S_L^{HLLC-LM} = \phi \cdot S_L, \qquad S_R^{HLLC-LM} = \phi \cdot S_R, \tag{13}$$

where $\phi = \sin\left(\min\left(1, \frac{Ma_{local}}{Ma_{limit}}\right) \cdot \frac{\pi}{2}\right)$ is a factor that smoothly reduces to zero for vanishing Mach numbers [9]. The HLLC-LM scheme reveals the same beneficial shock-stable properties as the Roe-M flux, while being considerable more robust for positivity-critical flow configurations. The right part of Figure 4 shows the beneficial stability exemplarily for the three-dimensional shock-driven bubble collapse of air in water.

2.6 | Time integration

The discretized evolution equation for the vector of conservative states (2) is integrated in time using the low-dissipation strongly stable third-order Runge–Kutta scheme

$$\begin{aligned} u^{(1)} &= u^{(n)} + \Delta t D\left(u^{(n)}\right) \\ u^{(2)} &= \frac{3}{4}u^{(n)} + \frac{1}{4}u^{(1)} + \frac{1}{4}\Delta t D\left(u^{(1)}\right) \\ u^{(n+1)} &= \frac{1}{3}u^{(n)} + \frac{2}{3}u^{(2)} + \frac{2}{3}\Delta t D\left(u^{(2)}\right), \end{aligned} \tag{14}$$

[14,16], where $D(u^*)$ abbreviates the discretization of the right-hand side. The numerical time-step size is restricted by various CFL criteria in the form of $\Delta t = f(\Delta x, \ldots)$ to ensure stability for the occurring physical effects (viscous fluxes, convective fluxes, heat fluxes, volume forces, and interface terms). As consequence of the dyadic grid refinement (2.3), a local time-stepping can be employed, where the actual time-step size is adjusted for each level of refinement to avoid using the smallest required time-step on the coarser cells. However, this approach can trigger numerical instabilities in the

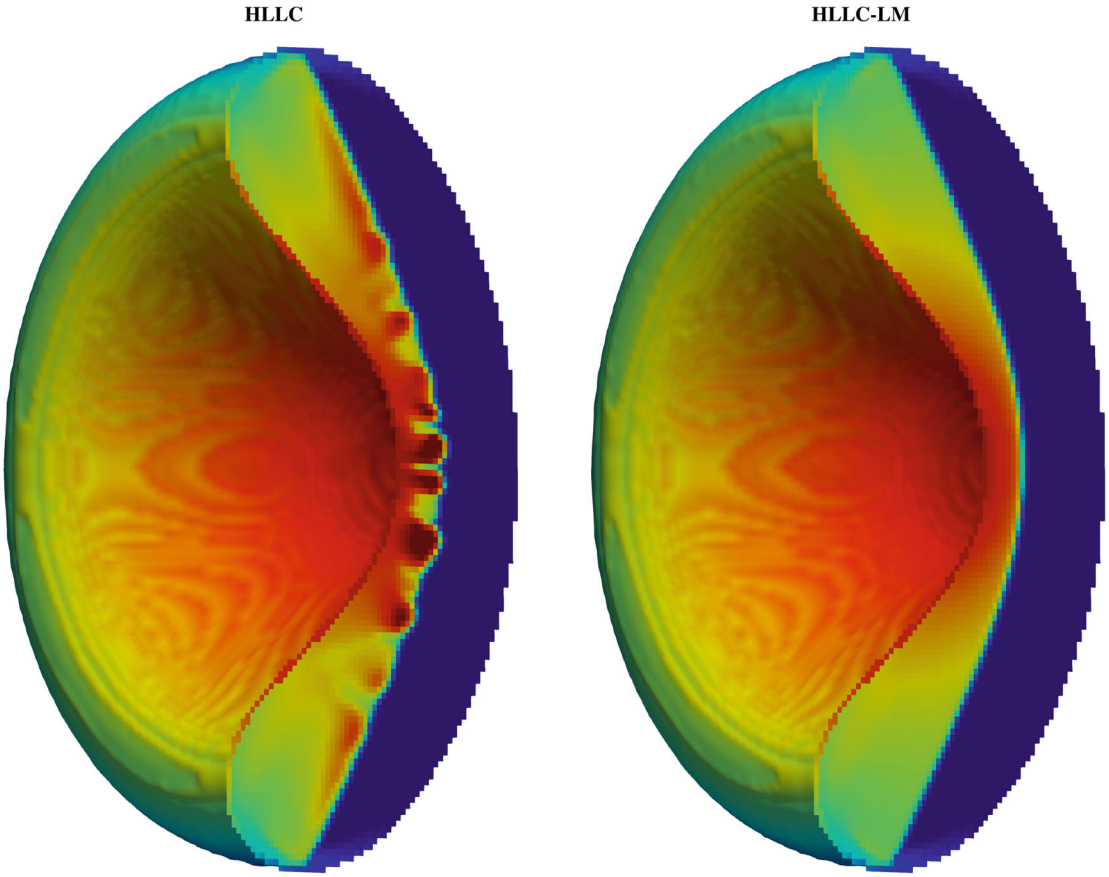

FIGURE 4 3D shock-driven bubble collapse of air in water with (left) and without (right) grid-aligned shock instability. Reprinted with permissions from the publisher.

presence of, for example, strong non-linear wave dynamics. As a remedy, we developed the adaptive local time stepping (ALTS) scheme [23] that significantly improves the robustness as compared to standard local time-stepping (LTS) schemes via a local time-step adaptation. ALTS allows to adapt the micro time step size to the present flow immediately, rather than only after a full macro cycle of a full Runge–Kutta stage on the coarsest level as with LTS. This is achieved the projection and prediction operations of the MR scheme on the numerical divergence of the flux vector rather than the conservative state vector. As an example, Figure 5 shows a snapshot of a non-symmetric shock-induced collapse of an air bubble near a rigid wall [20] simulated both with LTS (left) and ALTS (right). Clearly, the traditional LTS scheme introduces severe disturbances that break the simulations shortly after this snapshot. Due to the improved time-step size adaption, ALTS not only leads to improved stability of the simulations but also allows for higher CFL numbers.

2.7 | Level—set method

Numerical modeling of compressible multi-phase flows governs one of the most challenging problems in computational fluid dynamics. The presence of shock waves require low-dissipation schemes that allow to capture effectively discontinuous changes in the fluid state variables. Similarly, adjacent fluid phases can differ in their states and material properties by various orders of magnitudes. Physically, the interaction of shock waves with interfaces also can initiate the formation of new scales through baroclinic vorticity generation. These interface structures are smaller than the original reference scale, such as the bubble diameter, and require therefore adaptive meshing capabilities. Altogether, suitable numerical methods are required to introduce vanishing numerical effects like interface smearing or artificial viscosity. In this work, we focus on level set methods to describe the phase interfaces for their intrinsically sharp representation. Based on the original work of Osher and Sethian [26], level sets have been used for various applications like image segmentation [2], structural topology optimization [40] and, of course, for fluid interfaces [12] in both compressible and incompressible flows [34].

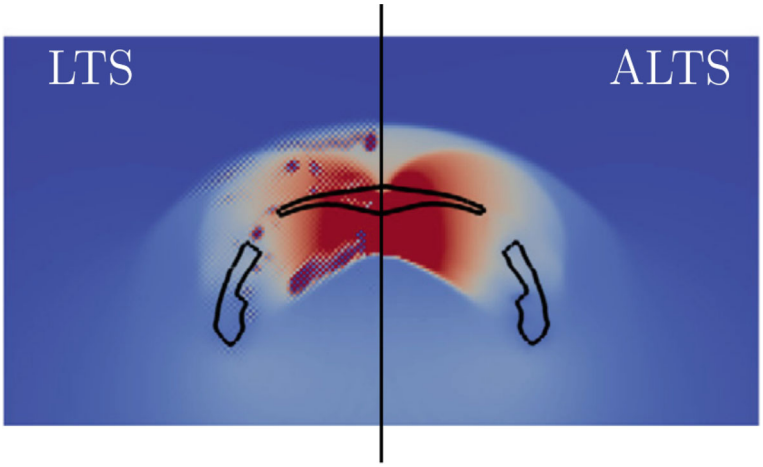

FIGURE 5 Shock-induced air bubble collapse in water simulated with traditional LTS (left) and ALTS (right). Reprinted with permissions under the terms of the Creative Commons CC-BY license.

The level-set function captures the interface implicitly by the zero level of the scalar field function $\phi(\mathbf{x}, t)$. Together with the signed-distance property $|\nabla\phi| = 1$, the geometry of the interface can be calculated from this scalar function [1,25]. When level sets are used to describe phase interfaces, in addition to the conservation equations also the level-set advection equation

$$\frac{\partial\phi}{\partial t} + \mathbf{u}_\Gamma \cdot \nabla\phi = 0, \tag{15}$$

is solved to evolve the phase interfaces in time. Note, $\mathbf{u}_\Gamma$ denotes the interface velocity of the level-set. It can be obtained from the contact-wave solution of a two-material Riemann problem at the phase interface and differs from the fluid velocity. Formally, the advection equation is only valid at the interface. However, we solve it in a small region around the interface. This slightly disturbs the signed-distance property of the level-set field. To restore the signed-distance property, we reinitialize the level-set field after every timestep [36]. The sharp representation of the interface allows to formulate conservative interaction terms between the fluids [19]. They require the interface pressures of both fluid. As the interface velocity, the interface pressures follow from the contact-wave solution of the two-material Riemann problem at the phase interface. Discretization of the single- and two-fluid equations requires knowledge of interface states and conservative states for both fluids in a small region around the interface. Therefore, we employ the ghost-fluid method [7] and extrapolate interface states and conservative states normal to the interface as described in [19]. To maintain the computational efficiency, we reduce the computational cost overhead of the level-set algorithm by narrow-band techniques [1,28] based on ideas of [3]. Therefrom, we deduce a smart tagging system to efficiently integrate the level-set treatment in the multiresolution algorithm [19].

3 | APPLICATION EXAMPLES

The combination of low-dissipation shock-capturing schemes with sharp interface models within an efficient multiresolution framework allows to simulate a broad range of interface-interaction driven applications. Here, we want to highlight three examples of a liquid–gas interface interaction with a strong density discontinuity, a gas–gas interface interaction, and a liquid–solid phase transition.

3.1 | Aerobreakup

Aerodynamic fragmentation describes the breakup of a drop into smaller droplets due to an ambient flow field. It plays an important role for a wide range of technical applications such as internal liquid-fuel combustion engines or manufacturing

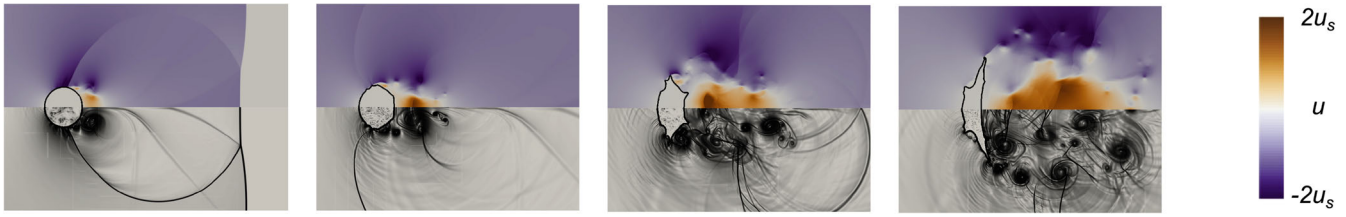

FIGURE 6 Normalized streamwise velocity (top) and numerical schlieren images (bottom) of the breakup of a water cylinder with diameter $D_0 = 4.8$ mm, initiated by a shock wave with $Ma_S = 1.47$. Shown are different time instants $t^* \in \{0.11, 0.19, 0.44, 0.76\}$ from left to right. Reprinted with permissions from the publisher.

or medical drugs [41]. The characteristics of the breakup process are governed by aerodynamic forces, viscous forces, and capillary effects. The two major non-dimensional numbers to describe the breakup process are the Weber number (We) and the Ohnesorge number. The former is defined as ratio of inertial to capillary forces, and the latter is defined as the ratio of viscous to capillary forces.

Theofanous [37] classifies the breakup based on the fundamental physical mechanisms which dominate the process: Rayleigh–Taylor piercing (RTP) and shear-induced entrainment (SIE). RTP can be observed for small Weber numbers and is dominated by the Rayleigh–Taylor instability. Thereby, after an initial flattening of the drop, Rayleigh–Taylor instabilities develop at the phase interface. The resulting waves penetrate the drop and lead to a bag-like deformation. SIE is the terminal instability mode for increasing Weber numbers and is governed by Kelvin–Helmholtz instabilites. This results in sheets stripping off the drop interface that might then be affected by local capillary breakups.

Numerical investigations of these phenomena pose special demands on the numerical solver. It has to be able to capture all relevant physical effects, the resulting instability patterns, and their interactions. In [21], we investigate the interface deformation dynamics in the SIE regime for a water column interacting with an ambient flow field. We highlight the importance to accurately resolve pressure waves near the phase interface and their interplay with instability-driven interfacial waves.

In Figure 6 we show the temporal evolution of a breakup process in the SIE regime. After shock-passage, the cylinder flattens and interface waves form at the equator ($t^* = 0.11$ and 0.19). These waves grow and finally form a hat-like structure on the upstream side of the cylinder ($t^* = 0.44$) and a sheet at the downstream part of the cylinder ($t^* = 0.76$). Along with the interface deformation, several regions with pronounced vortex shedding develop. After the initial shock passage, unsteady vortex shedding in the wake of the cylinder sets in and forms a recirculation zone ($t^* = 0.11$). Additional, smaller recirculation zones develop during the formation of the interfacial waves and lead to vortices shedding off from the equator ($t^* = 0.19$ and 0.44). Also, at the equatorial end of the hat-like structure and the developing sheet recirculation zones, eventually advecting downstream, develop ($t^* = 0.76$). Figure 7 shows good agreement between the simulation results and experimental visualizations of the SIE breakup mode.

The present simulation was conducted with an effective resolution of 200 cells per initial diameter. [21] show that fully resolving capillary waves with

$$We_\Delta = \frac{(\rho_l + \rho_{g,s}) u_{g,s}^2 \Delta x}{4\pi\sigma} \ll 1 \,, \tag{16}$$

where We_Δ is the cell Weber number [29], would require a resolution of approximately 3×10^5 cells per initial cylinder diameter. Thus, capillary disintegration of liquid sheets cannot be resolved by the simulations. Nevertheless, as the comparison with other experimental and numerical data in [21] suggests, the early stages of the breakup process are captured well by the simulations.

In [43], we increase the importance of capillary forces and simulate the case shown in the preceding for Weber number $We = 12$ in the RTP regime. We show the temporal evolution of the interface and flow field in Figure 8. After the initial shock passage, the drop flattens due to a non-uniform pressure distribution along the drop circumference [24]. As for the SIE, an interfacial wave develops at the drop equator. Due to the increasing importance of capillary effect, it is less pronounced for the RTP compared to the SIE. For later times ($t^* >= 1.0$), a wave pattern develops at the upstream side of the drop. Also, the onset of the growth of the bag-like shape, characteristic for the RTP regime, is visible ($t^* = 1.5$).

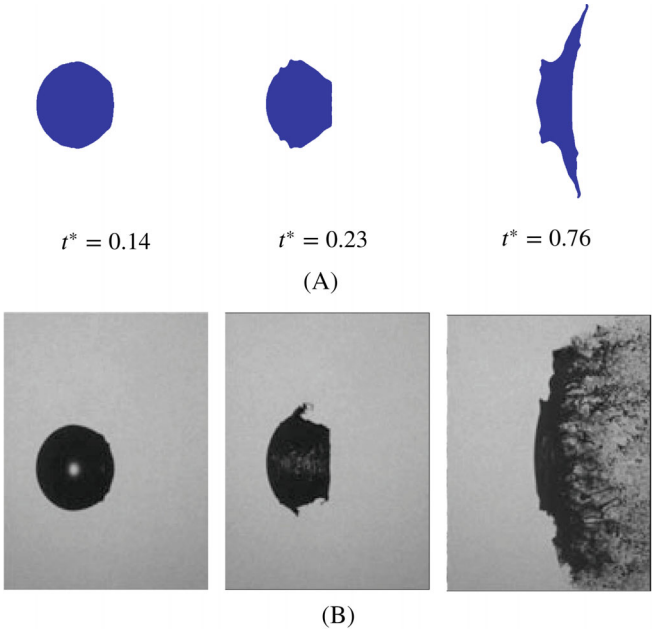

FIGURE 7 Qualitative comparison of the interface deformation process. The experimental figures are obtained from online-available videos. Reprinted from [38]. (A) Numerical results; (B) Experimental results of Theofanous [38]. Reprinted with permissions from the publisher.

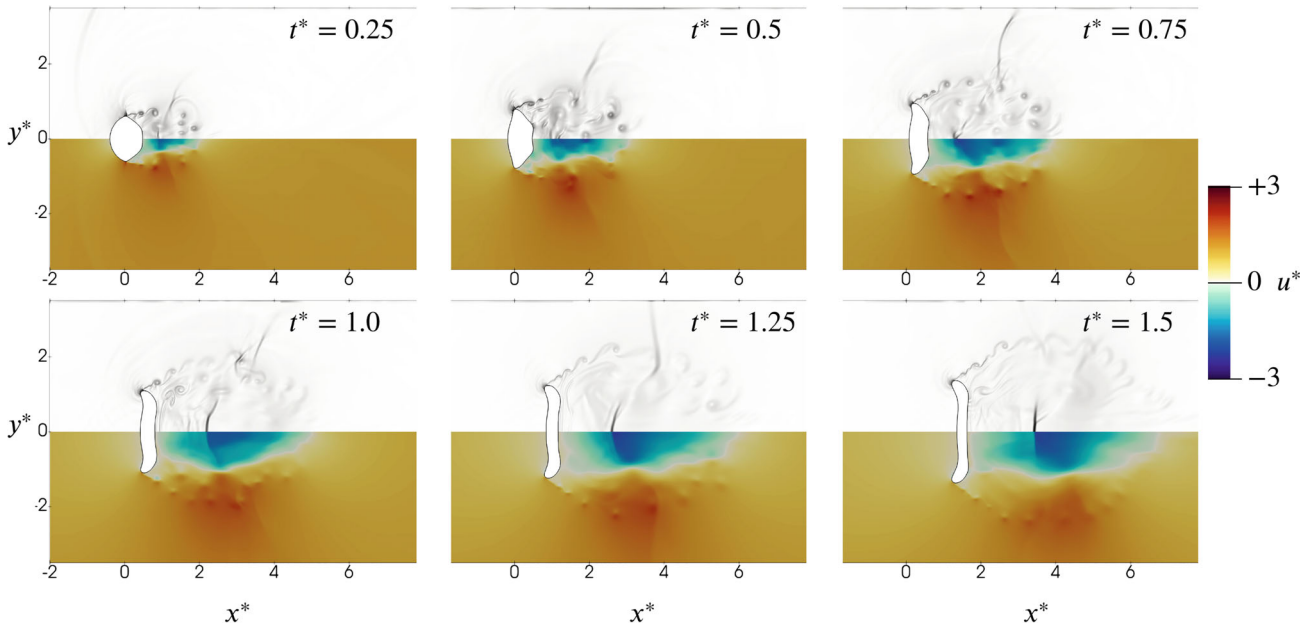

FIGURE 8 Numerical schlieren images (top) and normalized streamwise velocity (bottom) of the breakup of a water cylinder with diameter $D_0 = 4.8$ mm, initiated by a shock wave with $Ma_S = 1.47$. Shown are different time instants from left to right and top to bottom.

3.2 | Air R22 shock-bubble interaction

In contrast to the previous example, where we investigated a shock-interface interaction with strong density ratio, here, we consider a weaker density ratio. We present results for the interaction of a gaseous R22 sphere with a shock wave in air [19]. Also, we consider heat conduction and employ a Sutherland law to express the temperature dependence of viscosity for Air and R22. Figure 9 shows the temporal evolution of the shock-bubble interaction. The characteristics of the phase-interface deformation can be characterized by baroclinic vorticity generation at the interface, onset of interface

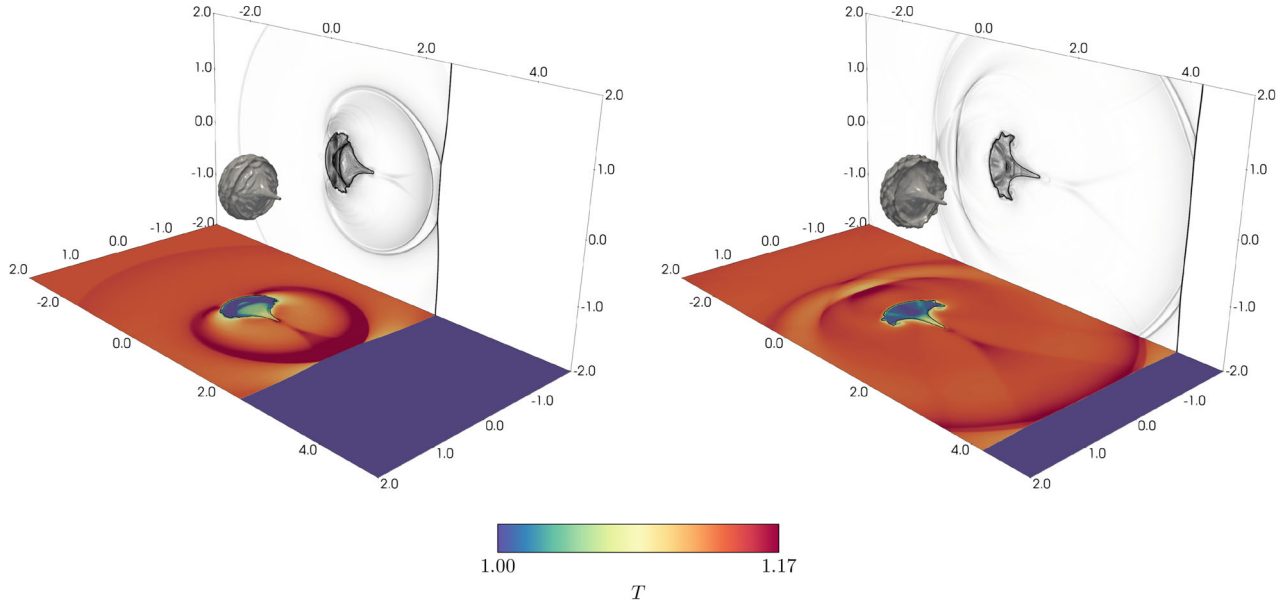

FIGURE 9 The flow field in the simulated domain and the interface contour. Shown are different time instants $t \in \{0.12, 0.18\}$ from left to right. Numerical schlieren in the x-y center place are projected to the upper right. Similarly, the temperature in the x-z center plane is shown in the bottom. The corresponding legend is given at the bottom. The contour of the R22 bubble is shown in gray. Light gray indicates a low interface velocity. Dark gray indicates a high interface velocity. Reprinted with permissions from the publisher.

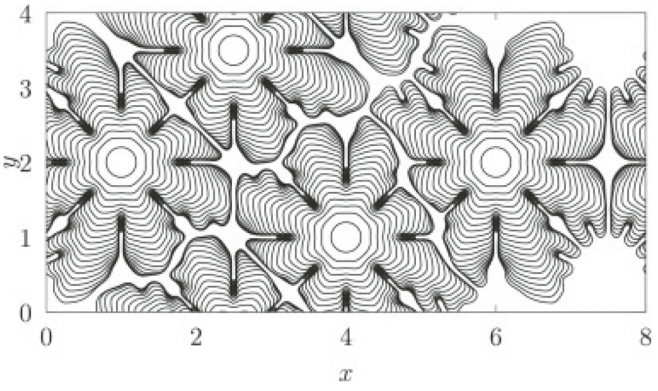

FIGURE 10 The solid–liquid interface for the growth of multiple crystals subjected to four-fold anisotropic surface tension in an undercooled liquid. Time increases as the interface extends from the initially spherical seeds. The time interval between two successive isolines is $\Delta t = 0.005$. Reprinted with permissions from the publisher.

perturbations, and shock-focusing phenomena inside the sphere. The focusing effects lead to a prolonged filament at the downstream side of the bubble.

3.3 | Solidification

Apart from *classical* compressible multiphase flow problems, level-set methods can be utilized to describe *any* propagating front. As such, Kaiser et al. [22] have extended the conservative interaction mechanism for liquid–solid phase transition to simulate crystal growth using a sharp interface description of the solidification front.

To capture the instability modes which occur during solidification of an undercooled liquid, a low-dissipation and accurate representation of the temperature field and the interface is required. Kaiser et al. [22] combined WENO-like reconstructions of interface gradients together with a semi-implicit level-set formulation to evolve the phase interface. The phase change model is formulated as conservative interface-exchange term at the moving front. They simulated the

growth of multiple crystals subjected to four-fold anisotropic surface tension in an undercooled liquid to mimic complex solidification microstructures. Figure 10 shows the growth of the multi-crystal configuration. The low-dissipative numerical model with accurate interface representation allows capturing the complex patterns developing at the phase interface. Also, the interplay between the multiple crystals and their interaction with the surrounding liquid is accurately captured by the method. Currently, this model is extended for binary mixtures to investigate more complex alloy solidification.

4 | CONCLUSIONS

We have presented an overview on latest developments for modeling compressible multi-phase flows using the sharp interface level set method. The simulation framework *ALPACA* combines latest multiresolution discretization schemes with low-dissipation shock-stable flux formulations to study immiscible fluid interactions. A collection of three representative examples demonstrates the capabilities of level sets for various physical problems including shock-interface interactions and crystal growth prediction. Further information on many details of the methods can be found in the original works and are provided in the respective sections.

AUTHOR CONTRIBUTIONS

Conceptualization: Stefan Adami. *Methodology*: Nico Fleischmann, Josef M. Winter, Stefan Adami, and Nikolaus A. Adams. *Software*: Nico Fleischmann and Josef M. Winter. *Writing - original draft preparation*: Nico Fleischmann, Josef M. Winter, and Stefan Adami. *Writing - review and editing*: Nico Fleischmann, Josef M. Winter, Stefan Adami, and Nikolaus A. Adams. *Supervision*: Stefan Adami and Nikolaus A. Adams. *Funding acquisition*: Nikolaus A. Adams.

ACKNOWLEDGEMENTS

The authors acknowledge funding from the European Research Council (ERC) under the European Union's Horizon 2020 research and innovation program (Grant agreement No. 667483). The authors gratefully acknowledge the Gauss Centre for Supercomputing e.V. (http://www.gauss-centre.eu) for funding this project by providing computing time on the GCS Supercomputer SuperMUC at Leibniz Supercomputing Centre (http://www.lrz.de). Open access funding enabled and organized by Projekt DEAL. [Correction added on 23 September 2022, after first online publication: Projekt Deal funding statement has been added.]

CONFLICT OF INTEREST

The authors declare no potential conflict of interests.

REFERENCES

[1] D. Adalsteinsson and J. A. Sethian, A fast level set method for propagating interfaces, J. Comput. Phys. **118** (1995), no. 2, 269–277.
[2] S. Biswas and R. Hazra, State-of-the-art level set models and their performances in image segmentation: A decade review, Arch. Comput. Methods Eng. (2021). https://doi.org/10.1007/s11831-021-09646-y.
[3] D. Chopp, Computing minimal surfaces via level set curvature flow, J. Comput. Phys. **106** (1993), no. 1, 77–91.
[4] R. Deiterding, M. O. Domingues, and K. Schneider, Multiresolution analysis as a criterion for effective dynamic mesh adaptation – A case study for euler equations in the samr framework amroc, Comput. Fluids **205** (2020), 104583.
[5] W. S. Don, P. Li, K. Y. Wong, and Z. Gao, Improved symmetry property of high order weighted essentially non-oscillatory finite difference schemes for hyperbolic conservation laws, Adv. Appl. Math. Mech. **10** (2018), no. 6, 1418–1439.
[6] W. S. Don, D. M. Li, Z. Gao, and B. S. Wang, A characteristic-wise alternative weno-z finite difference scheme for solving the compressible multicomponent non-reactive flows in the overestimated quasi-conservative form, J. Sci. Comput. **82** (2020), no. 2, 1–24.
[7] R. P. Fedkiw, T. Aslam, B. Merriman, and S. Osher, A non-oscillatory Eulerian approach to interfaces in multimaterial flows (The ghost fluid method), J. Comput. Phys. **152** (1999), no. 2, 457–492.
[8] N. Fleischmann, S. Adami, and N. A. Adams, Numerical symmetry-preserving techniques for low-dissipation shock-capturing schemes, Comput. Fluids **189** (2019), 94–107.
[9] N. Fleischmann, S. Adami, and N. A. Adams, A shock-stable modification of the hllc riemann solver with reduced numerical dissipation, J. Comput. Phys. **423** (2020), 109762.
[10] N. Fleischmann, S. Adami, X. Y. Hu, and N. A. Adams, A low dissipation method to cure the grid-aligned shock instability, J. Comput. Phys. **401** (2020), 109004.
[11] L. Fu, X. Y. Hu, and N. A. Adams, A family of high-order targeted eno schemes for compressible-fluid simulations, J. Comput. Phys. **305** (2016), 333–359.
[12] F. Gibou, R. Fedkiw, and S. Osher, A review of level-set methods and some recent applications, J. Comput. Phys. **353** (2018), 82–109. https://www.sciencedirect.com/science/article/pii/S0021999117 307441

[13] S. K. Godunov, A difference method for numerical calculation of discontinuous solutions of the equations of hydrodynamics, Mat. Sb. **89** (1959), no. 3, 271–306.
[14] S. Gottlieb, C.-W. Shu, and E. Tadmor, Strong stability-preserving high-order time discretization methods, SIAM Rev. **43** (2001), no. 1, 89–112.
[15] A. Harten, Multiresolution algorithms for the numerical solution of hyperbolic conservation laws, Commun. Pure Appl. Math. **48** (1995), no. 12, 1305–1342.
[16] A. Harten, P. D. Lax, and B. Van Leer, On upstream differencing and Godunov-type schemes for hyperbolic conservation laws, SIAM Rev. **25** (1983), no. 1, 35–61.
[17] Hoppe N, Adami S, Adams NA. A modular massively parallel computing environment for three-dimensional multiresolution simulations of compressible flows; 2020.
[18] N. Hoppe, S. Adami, NA. Adams, I. Pasichnyk, and M. Allalen, *Node-level optimization of a 3D block-based multiresolution compressible flow solver with emphasis on performance portability*, Proc. 2019 Int. Conf. High Perform. Comput. Simul. (HPCS), 2019, Dublin, Ireland, pp. 732–740, https://doi.org/10.1109/HPCS48598.2019.9188088.
[19] N. Hoppe, J. M. Winter, S. Adami, N. A. Adams, Alpaca - a level-set based sharp-interface multiresolution solver for conservation laws, Comput. Phys. Commun. **272** (2022), 108246. https://www.sciencedirect.com/science/article/pii/S0010465521003581
[20] E. Johnsen and T. Colonius, Numerical simulations of non-spherical bubble collapse, J. Fluid Mech. **629** (2009), 231–262.
[21] Kaiser JW, Winter JM, Adami S, Adams NA. Investigation of interface deformation dynamics during high-weber number cylindrical droplet breakup, Int. J. Multiphase Flow **132** (2020), 103409. https://www.sciencedirect.com/science/article/pii/S0301932220305188
[22] J. W. Kaiser, S. Adami, I. S. Akhatov, and N. A. Adams, A semi-implicit conservative sharp-interface method for liquid-solid phase transition, Int. J. Heat Mass Transf. **155** (2020), 119800.
[23] J. W. Kaiser, N. Hoppe, S. Adami, and N. A. Adams, An adaptive local time-stepping scheme for multiresolution simulations of hyperbolic conservation laws, J. Comput. Phys. X **4** (2019), 100038.
[24] J. C. Meng and T. Colonius, Numerical simulations of the early stages of high-speed droplet breakup, Shock Waves **25** (2015), 339–414.
[25] S. Osher and R. P. Fedkiw, Level set methods: An overview and some recent results, J. Comput. Phys. **169** (2001), no. 2, 463–502.
[26] S. Osher and J. A. Sethian, Fronts propagating with curvature-dependent speed: Algorithms based on Hamilton-jacobi formulations, J. Comput. Phys. **79** (1988), no. 1, 12–49.
[27] K. Peery and S. Imlay, *Blunt-body flow simulations*, Proc. 24th Joint Propuls, Conf, Boston, MA, Vol. 2904, 1988.
[28] D. Peng, B. Merriman, S. Osher, H. Zhao, and M. Kang, A pde-based fast local level set method, J. Comput. Phys. **155** (1999), no. 2, 410–438.
[29] S. Popinet, Numerical models of surface tension, Annu. Rev. Fluid Mech. **50** (2018), no. 1, 49–75.
[30] J. J. Quirk, "A Contribution to the Great Riemann Solver Debate." In: M. Y. Hussaini, B. van Leer, and J. Van Rosendale (eds.), *Upwind and High-Resolution Schemes*. Springer, Berlin, Heidelberg. https://doi.org/10.1007/978-3-642-60543-7_22
[31] J.-F. Remacle, J. E. Flaherty, and M. S. Shephard, An adaptive discontinuous Galerkin technique with an orthogonal basis applied to compressible flow problems, SIAM Rev. **45** (2003), no. 1, 53–72.
[32] A. V. Rodionov, Artificial viscosity in Godunov-type schemes to cure the carbuncle phenomenon, J. Comput. Phys. **345** (2017), 308–329.
[33] P. L. Roe, Approximate Riemann solvers, parameter vectors, and difference schemes, J. Comput. Phys. **43** (1981), no. 2, 357–372.
[34] J. A. Sethian and P. Smereka, Level set methods for fluid interfaces, Annu. Rev. Fluid Mech. **35** (2003), no. 1, 341–372.
[35] C.-W. Shu and S. Osher, Efficient implementation of essentially non-oscillatory shock-capturing schemes, J. Comput. Phys. **77** (1988), no. 2, 439–471.
[36] M. Sussman, P. Smereka, and S. Osher, A level set approach for computing solutions to incompressible two-phase flow, J. Comput. Phys. **114** (1994), 146–159.
[37] T. Theofanous, Aerobreakup of Newtonian and viscoelastic liquids, Annu. Rev. Fluid Mech. **43** (2011), no. 1, 661–690.
[38] T. G. Theofanous, V. V. Mitkin, C. L. Ng, C. H. Chang, X. Deng, and S. Sushchikh, The physics of aerobreakup. Part II. Viscous liquids, Phys. Fluids **24** (2012), 022104.
[39] E. F. Toro, M. Spruce, and W. Speares, Restoration of the contact surface in the HLL-Riemann solver, Shock Waves **4** (1994), no. 1, 25–34.
[40] N. P. van Dijk, K. Maute, M. Langelaar, and F. van Keulen, Level-set methods for structural topology optimization: A review, Struct. Multidiscipl. Optim. **48** (2013), no. 3, 437–472. https://doi.org/10.1007/s00158-013-0912-y.
[41] E. Villermaux, Fragmentation, Annu. Rev. Fluid Mech. **39** (2007), 419–446.
[42] B.-S. Wang, W. S. Don, N. K. Garg, and A. Kurganov, Fifth-order a-weno finite-difference schemes based on a new adaptive diffusion central numerical flux, SIAM J. Sci. Comput. **42** (2020), no. 6, A3932–A3956.
[43] J. M. Winter, J. W. Kaiser, S. Adami, and N. A. Adams, *Numerical investigation of 3D drop-breakup mechanisms using a sharp interface level-set method*, Proc. 11th Int. Sympos. Turbul. Shear Flow Phenomena, TSFP, Southampton, UK, 2019. https://mediatum.ub.tum.de/1522845.

How to cite this article: N. Fleischmann, J. M. Winter, S. Adami, and N. A. Adams, *High-order modeling of interface interactions using level sets*, GAMM-Mitteilungen. **45** (2022), e202200012. https://doi.org/10.1002/gamm.202200012